

Article

Structural Phase Transition and Related Thermoelectric Properties in Sn Doped AgBiSe₂

Xiao-Cun Liu ^{1,*}  and Ming-Yan Pan ²¹ School of Civil Engineering, Shandong Jiaotong University, Jinan 250023, China² Key Laboratory of Materials for High Power Laser, Shanghai Institute of Optics and Fine Mechanics, Chinese Academy of Sciences, Shanghai 201800, China; pmy@siom.ac.cn

* Correspondence: liuxiaocunde@163.com

Abstract: AgBiSe₂, which exhibits complex structural phase transition behavior, has recently been considered as a potential thermoelectric material due to its intrinsically low thermal conductivity. In this work, we investigate the crystal structure of Sn-doped AgBiSe₂ through powder X-ray diffraction and differential scanning calorimetry measurements. A stable cubic Ag_{1-x/2}Bi_{1-x/2}Sn_xSe₂ phase can be obtained at room temperature when the value of x is larger than 0.2. In addition, the thermoelectric properties of Ag_{1-x/2}Bi_{1-x/2}Sn_xSe₂ ($x = 0.2, 0.25, 0.3, 0.35$) are investigated, revealing that Ag_{1-x/2}Bi_{1-x/2}Sn_xSe₂ compounds are intrinsic semiconductors with a low lattice thermal conductivity. This work provides new insights into the crystal structure adjustment of AgBiSe₂ and shows that Ag_{1-x/2}Bi_{1-x/2}Sn_xSe₂ is a potentially lead-free thermoelectric material candidate.

Keywords: crystal structure; thermoelectric property; Seebeck coefficient; thermal conductivity



Citation: Liu, X.-C.; Pan, M.-Y. Structural Phase Transition and Related Thermoelectric Properties in Sn Doped AgBiSe₂. *Crystals* **2021**, *11*, 1016. <https://doi.org/10.3390/cryst11091016>

Academic Editors: Ady Suwardi, Yun Zheng and Bhuvanesh Srinivasan

Received: 29 July 2021

Accepted: 23 August 2021

Published: 25 August 2021

Publisher's Note: MDPI stays neutral with regard to jurisdictional claims in published maps and institutional affiliations.



Copyright: © 2021 by the authors. Licensee MDPI, Basel, Switzerland. This article is an open access article distributed under the terms and conditions of the Creative Commons Attribution (CC BY) license (<https://creativecommons.org/licenses/by/4.0/>).

1. Introduction

As devices that can convert heat and electricity, thermoelectric devices have received significant attention and have become a research hotspot in recent years [1–3]. The thermoelectric properties of materials can be evaluated by using the dimensionless quantity ZT . The value of ZT can be calculated with the formula $S^2\sigma T / (\kappa_{\text{ele}} + \kappa_{\text{latt}})$, where S , σ , T , κ_{ele} , and κ_{latt} are the Seebeck coefficient, electrical conductivity, temperature, electronic thermal conductivity, and lattice thermal conductivity, respectively. Accordingly, semiconductors with low lattice thermal conductivities have been widely studied and show excellent thermoelectric performance. These semiconductors include Zintl phases [4,5], fast ion conductors [6,7], complex oxides [8,9], and chalcogenides [10].

Ternary chalcogenides with the I-V-VI₂ formula (I = Cu, Ag; V = As, Sb, Bi; VI = S, Se, Te) have an intrinsically ultra-low lattice thermal conductivity due to their unique crystal structures [11–13]. For example, due to the anharmonicity caused by the repulsion between neighboring chalcogen ions and lone-pair electrons, the lattice thermal conductivity of CuSbS₂ is only about 0.5 W·m⁻¹·K⁻¹ at 627 K [14]. In AgSbSe₂ and AgSbTe₂, the mixing of Ag and Sb atoms can lead to a further decline in lattice thermal conductivity [15–18]. I-V-VI₂ compounds have a wide range of structural diversity. The crystal structure of Cu-containing compounds such as CuSbS₂ and CuSbSe₂ can be viewed as the stacking of [CuSb(S/Se)₂] layers in an A \bar{A} A \bar{A} -type sequence along the c axis direction [19,20]. AgSbSe₂ and AgSbTe₂ crystallize in the cubic space group Fm $\bar{3}$ m with disordered Ag and Sb cations [21], while AgBiVI₂ (VI = S, Se, Te) compounds exhibit complex temperature-dependent phase transition behavior [22–25].

AgBiSe₂ compound exists in three polymorphs: a disordered cubic phase, an ordered hexagonal phase, and a rhombohedral phase. Their structures are shown in Figure 1. As an n-type semiconductor with poor electrical conductivity, the thermoelectric properties of AgBiSe₂ can be enhanced by increasing the charge carrier concentration via doping In, Nb, or Ge at Ag sites [26–28] or by doping halogen elements at Se sites [29]. Both experimental

and density functional theory calculation results indicate that *p*-type hexagonal AgBiSe₂ can potentially be used in room-temperature thermoelectric applications [30,31]. Additionally, the phase transition temperatures of AgBi_{1-x}Sb_xSe₂ are determined by the doping concentration of Sb [32,33]. Very recently, Br-doped cubic (AgBiSe₂)_{0.7}(PbSe)_{0.3} phase has been proved to be potential material with fine thermoelectric properties in the range from 300 to 800 K [34]. The stable cubic AgBiSe₂ phase may potentially exhibit excellent thermoelectric properties due to its intrinsic crystal structures and related electronic structures. The high symmetry can result in energy band degeneracy, and thus lead to high power factor, while the material with disordered atoms usually exhibits ultra-low lattice thermal conductivity [35]. Accordingly, further investigation into methods for achieving a stable cubic AgBiSe₂ phase and enhancing its thermoelectric properties are of great interest.

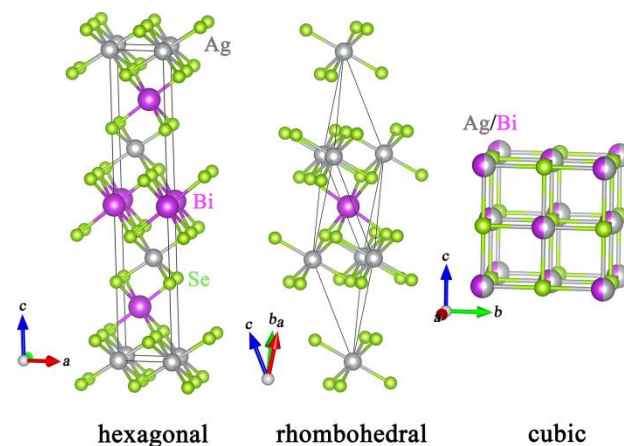


Figure 1. Crystal structures of the hexagonal, rhombohedral, and cubic phases of AgBiSe₂.

Inspired by the research on (AgBiSe₂)_{1-x}(PbSe)_x, we focus on another IV-A metal and find that a stabilized room-temperature cubic AgBiSe₂ phase can also be achieved via Sn substitution. In previous studies, both AgSbSe₂ and PbSe have cubic crystal structures, so it is not hard to understand the phase transition behavior in (AgBiSe₂)_{1-x}(AgSbSe₂)_x and (AgBiSe₂)_{1-x}(PbSe)_x solid solutions [32–34]. Herein, although the crystal structure of SnSe is not cubic [36], the solid solution between SnSe and AgBiSe₂ has a cubic structure at room temperature. Such a finding indicates that in-depth studies on structural phase transition and its related physical properties are needed. In addition, in this work the thermoelectric properties were also investigated, and the results indicate that Ag_{1-x/2}Bi_{1-x/2}Sn_xSe₂ is a potentially lead-free thermoelectric material with ultra-low lattice thermal conductivity.

2. Materials and Methods

Ag_{1-x/2}Bi_{1-x/2}Sn_xSe₂ samples were prepared via high-temperature solid-state reactions. Stoichiometric amounts of Ag (Alfa, 99.9%), Bi (Aladdin, 99.999%), Sn (Alfa, 99.99%), and Se (Alfa, 99.99%) were cut into small pieces and weighed in an argon-filled glovebox. The elements were mixed and loaded into evacuated silica tubes. The tubes were then heated to 1273 K at a rate of 80 K/h and homogenized at this temperature for 20 h using a programmable furnace. Finally, the tubes were slowly cooled down to room temperature over 20 h. The synthesized ingots were ground into fine powders for use in further measurements.

Powder X-ray diffraction (PXRD) patterns of Ag_{1-x/2}Bi_{1-x/2}Sn_xSe₂ were measured with a step size of 0.02° by using a Bruker D8 Advance X-ray powder diffractometer at room temperature and Cu Kα radiation. Rietveld refinements of AgBiSe₂, Ag_{0.975}Bi_{0.975}Sn_{0.05}Se₂, and Ag_{0.95}Bi_{0.95}Sn_{0.10}Se₂ were performed using Fullprof [37]. Differential scanning calorimetry (DSC) measurements were performed on the polycrystalline powders of Ag_{1-x/2}Bi_{1-x/2}Sn_xSe₂ (35–45 mg) using a NETZSCH STA 449 F3. DSC measurements were taken over a temperature range of 350 K to 650 K. The heating rate was 10 K/min. The

microstructure and energy-dispersive spectroscopy (EDS) mapping of $\text{Ag}_{0.90}\text{Bi}_{0.90}\text{Sn}_{0.20}\text{Se}_2$ sample were carried out using a Zeiss Sigma 500 field emission scanning electron microscopy (SEM).

$\text{Ag}_{1-x/2}\text{Bi}_{1-x/2}\text{Sn}_x\text{Se}_2$ ($x = 0.2, 0.25, 0.3, 0.35$) powders were sintered into pellets with high relative densities by using a LABOX-325 spark plasma sintering instrument (Dr. Sinter Land). An axial compressive stress of 40 MPa was applied at 773 K for 7 min under 10 Pa. The Seebeck coefficients and electrical conductivity values at temperatures of 300 K to 773 K were measured using a NETZSCH SBA 458 instrument with a temperature gradient of 4 K across ~ 8.25 mm. Thermal conductivity was calculated using the standard formula $\kappa = C_p D \rho$, where C_p is the specific heat calculated by the Dulong-Petit law, D is the thermal diffusivity measured using the laser flash method (NETZSCH LFA 457), and ρ is the measured mass density.

3. Results and Discussion

Theoretical diffraction patterns for hexagonal, rhombohedral, and cubic AgBiSe_2 are shown in Figure 2a, while Figure 2b shows PXRD patterns for $\text{Ag}_{1-x/2}\text{Bi}_{1-x/2}\text{Sn}_x\text{Se}_2$ ($x = 0, 0.1, 0.15, 0.2, 0.25, 0.30, 0.35$). The measured diffraction patterns of AgBiSe_2 are completely consistent with the theoretical patterns of the hexagonal phase, indicating that the pristine AgBiSe_2 is phase pure. The diffraction patterns change with increasing Sn concentration in the Sn-doped compounds. For instance, the (110) diffraction pattern at 43.26° and (018) diffraction pattern at 44.52° become closer with an increasing Sn ratio. Meanwhile, some small patterns such as (003) at 13.5° , (101) at 24.98° , and (006) at 27.18° disappear when x is higher than 0.15. The PXRD patterns for the samples with high Sn concentrations are similar to the theoretical diffraction patterns of cubic AgBiSe_2 , revealing that a stable cubic phase can be achieved at room temperature via Sn doping. There are no impurity patterns in the measured data, indicating that solid solutions were formed in all the samples. It should be noticed that although the diffraction patterns of $\text{Ag}_{0.925}\text{Bi}_{0.925}\text{Sn}_{0.15}\text{Se}_2$ are consistent with the cubic phase, the broad pattern at about 43.82° potentially hints that $\text{Ag}_{0.925}\text{Bi}_{0.925}\text{Sn}_{0.15}\text{Se}_2$ is an intermediate phase between the hexagonal and cubic phases. Accordingly, only the thermoelectric properties of cubic $\text{Ag}_{1-x/2}\text{Bi}_{1-x/2}\text{Sn}_x\text{Se}_2$ ($x = 0.2, 0.25, 0.3, 0.35$) are discussed in this paper.

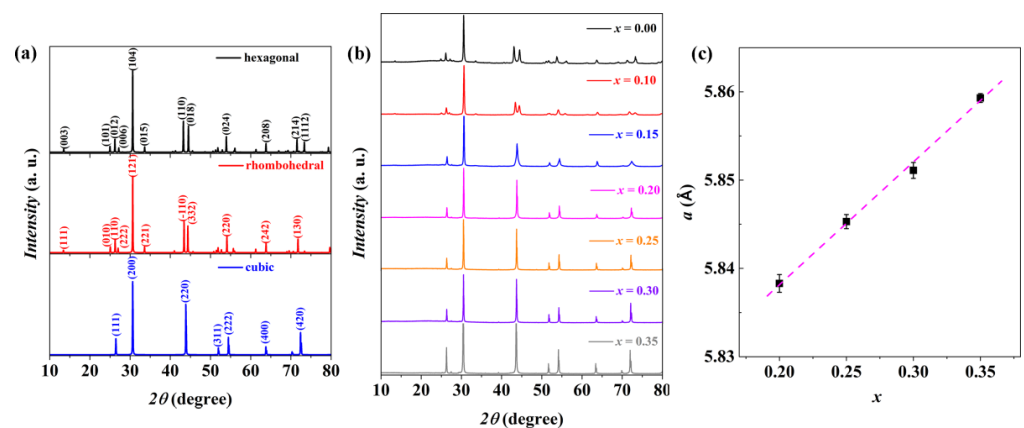


Figure 2. (a) Theoretical diffraction patterns for hexagonal, rhombohedral, and cubic phase AgBiSe_2 . Patterns are labeled with their primary crystal indices. (b) Experimental diffraction patterns of $\text{Ag}_{1-x/2}\text{Bi}_{1-x/2}\text{Sn}_x\text{Se}_2$ ($x = 0, 0.10, 0.15, 0.20, 0.25, 0.30, 0.35$). (c) Calculated lattice parameters (a) from the PXRD results vs. Sn concentration (x). The dashed line indicates the best linear fit of the lattice parameters.

As shown in Figure 2c, the lattice parameters determined from the experimental PXRD patterns increase linearly with increasing Sn concentration. This is consistent with Vegard's law. In general, variations in the lattice parameter of chalcogenide semiconductors

can be explained by ionic radius differences between the intrinsic and doped elements. Since the ionic radius of Sn^{2+} is difficult to define [38], the increased lattice parameter cannot be directly explained by comparing ionic radii. However, a cubic SnSe phase which crystallizes in a rock salt structure may potentially help understand this change in lattice parameter [39]. The Sn-Se bonding distance in cubic SnSe is about 2.995 Å, much longer than the Ag/Bi-Se distance of 2.916 Å in cubic AgBiSe₂. Thus, the ionic radius of Sn^{2+} in the rock salt structure should be larger than the average ionic radius between Ag^+ and Bi^{3+} .

DSC measurements were performed for $\text{Ag}_{1-x/2}\text{Bi}_{1-x/2}\text{Sn}_x\text{Se}_2$ ($x = 0, 0.05, 0.10, 0.15, 0.20, 0.25, 0.30$) in order to understand the polymorph change at room temperature. The results are shown in Figure 3. For pristine AgBiSe₂, one small peak at about 500 K indicates the phase transition from a hexagonal to a rhombohedral phase, while the sharp peak at 586 K represents the transformation to a cubic phase. For Sn-containing materials, the temperature corresponding to the sharp endothermic peak decreases with increasing Sn concentrations. Therefore, the thermal energy required to overcome the potential energy between the hexagonal and cubic phases also decreases. For $\text{Ag}_{0.925}\text{Bi}_{0.925}\text{Sn}_{0.15}\text{Se}_2$, a small and flat endothermic peak at about 520 K indicates the existence of the hexagonal phase, consistent with the prior discussion of PXRD data. The finding is interesting since neither AgBiSe₂ nor SnSe has a cubic structure at room temperature. Accordingly, in order to understand the phenomenon, detailed analysis of the crystal structures for Ag-V-Se ($V = \text{As}, \text{Sb}, \text{Bi}$) compounds was performed.

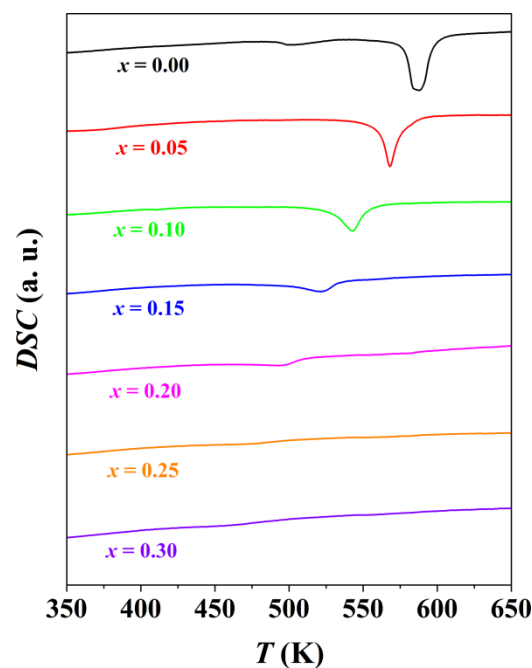


Figure 3. DSC curves for $\text{Ag}_{1-x/2}\text{Bi}_{1-x/2}\text{Sn}_x\text{Se}_2$ ($x = 0, 0.05, 0.10, 0.15, 0.20, 0.25, 0.30$) samples in the range of 350 K to 650 K. The endothermic direction is downward in the figure.

AgBiSe₂ shows multiple crystal phase transitions with increasing temperature, transforming from ordered hexagonal $P\bar{3}m1$ to rhombohedral $R\bar{3}mR$ and then to the disordered rock salt structure [21]. AgSbSe₂ is a cubic phase material with mixed Ag and Sb atoms [21], while AgAsSe₂ crystallizes in the rhombohedral space group $R\bar{3}mH$ [40]. Although these compounds crystallize in different space groups, their crystal structures are very similar, as shown in Figure 4. It is clear that the difference between Ag-Se and V-Se bonding distances plays a major role in determining the crystal structure of Ag-V-Se materials. In order to describe the bonding distance difference simply, the ratios between average Ag-Se and V-Se bonding distances in octahedrons are shown in the figure. The ratios of $r_{\text{avg}}(\text{Ag-Se})/r_{\text{avg}}(\text{V-Se})$ for AgBiSe₂, AgSbSe₂ and AgAsSe₂ are 0.95, 1.00, and 1.09, respectively. The ratios affect the Se-V-Se angle directly, and further determine the

distortion degree of the octahedral environments. The longer Bi-Se distance in AgBiSe₂ leads to a Se-Bi-Se angle of 87.2°. In contrast, the shorter As-Se distance of 2.710 Å in AgAsSe₂ results in a larger Se-As-Se angle (92.5°). Accordingly, for AgVSe₂ compounds, adjustment of Ag-Se and V-Se distances can change the crystal structure. The Sn-Se bonding distance is longer than the Ag-Se distances but shorter than the Bi-Se distances. In Ag_{1-x/2}Bi_{1-x/2}Sn_xSe₂, the bonding distance difference between Ag/Sn-Se and Bi/Sn-Se decreases with increasing Sn ratio. So the crystal structure of AgBiSe₂ can be transformed to cubic phase via Sn doping. The Rietveld refinement results of Ag_{1-x/2}Bi_{1-x/2}Sn_xSe₂ (x = 0, 0.05, 0.10) are consistent with the above analysis. As is shown in Figure S1, the Se-Bi-Se angle increases with increasing x value. Considering that these structures are extremely complex, further experimental studies on the crystal structures of metal-doped AgBiVI₂ (VI = S, Se, Te) are still needed.

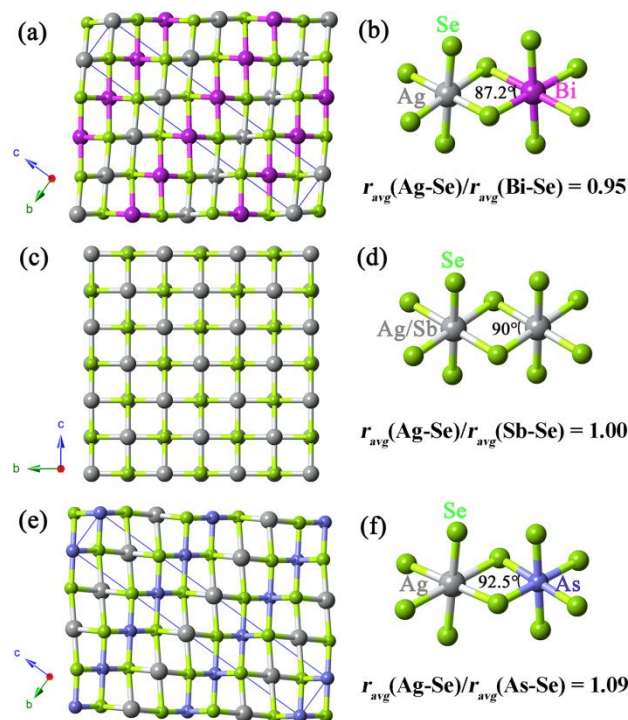


Figure 4. Ball-and-stick representation of (a) hexagonal AgBiSe₂, (c) AgSbSe₂, and (e) AgAsSe₂. Ball-and-stick views of fragments showing the connection between [AgSe₆] and (b) [BiSe₆], (d) [SbSe₆], and (f) [AsSe₆] octahedrons. The $r_{\text{avg}}(\text{Ag-Se})$, $r_{\text{avg}}(\text{Bi-Se})$, $r_{\text{avg}}(\text{Sb-Se})$ and $r_{\text{avg}}(\text{As-Se})$ in the figure are average bonding distances of Ag-Se, Bi-Se, Sb-Se and As-Se in octahedrons, respectively.

As shown in Figure S2, there is no obvious pore or crack in the cross-sectional image, suggesting high density of the sintered sample. The distribution for all elements is homogeneous, indicating that the material is phase pure. Figure 5 shows the measured temperature-dependent thermoelectric transport properties of Ag_{1-x/2}Bi_{1-x/2}Sn_xSe₂. Tin doping leads to significant changes in both the Seebeck coefficient and electrical conductivity. Due to the phase transition behaviour, both Seebeck coefficient and electrical conductivity of pristine AgBiSe₂ do not change monotonically with increasing temperature. Pristine AgBiSe₂ is an intrinsic n-type semiconductor with a negative Seebeck coefficient over the entire measured temperature range. The Seebeck coefficients of the Sn-doped materials are positive at room temperature, indicating that the dominating charge carriers are holes. The room-temperature Seebeck coefficient of Ag_{0.90}Bi_{0.90}Sn_{0.20}Se₂ is about +130 μV/K, while that of Ag_{0.875}Bi_{0.875}Sn_{0.25}Se₂ increases to about +350 μV/K. A similar carrier type transition behaviour has been observed in AgBi_{1-x}Sb_xSe₂ [33,34]. With increasing temperature, the Seebeck coefficients of the Ag_{1-x/2}Bi_{1-x/2}Sn_xSe₂ samples are converted into n-type negative values. The carrier type change from p-type to n-type can be at-

tributed to the thermally generated extrinsic carriers at high temperatures. The absolute value of the Seebeck coefficients in the high-temperature region decreases with increasing Sn content. With increasing temperature, the electrical conductivity of all materials exponentially increases, indicating that the cubic crystal structure Sn-doped materials are intrinsic semiconductors. As shown in Figure S3, the logarithmic plot of ρ in the high temperature region versus the inverse temperature show linearity. According to the thermal activation model, the energy band gaps for all Sn-doped samples are calculated using the formula $\ln \rho_T = E_g/2k_B T + f$, where E_g is the band gap, T is the absolute temperature, and k_B is the Boltzmann constant. The band gaps deduced from thermal activation model for $\text{Ag}_{0.90}\text{Bi}_{0.90}\text{Sn}_{0.20}\text{Se}_2$, $\text{Ag}_{0.875}\text{Bi}_{0.875}\text{Sn}_{0.25}\text{Se}_2$, $\text{Ag}_{0.85}\text{Bi}_{0.85}\text{Sn}_{0.30}\text{Se}_2$ and $\text{Ag}_{0.825}\text{Bi}_{0.825}\text{Sn}_{0.35}\text{Se}_2$ are 0.63 eV, 0.47 eV, 0.42 eV and 0.38 eV, respectively. The band gap gradually decreases with the increasing Sn ratio. In addition, in contrast to the changes to the Seebeck coefficients, the electrical conductivity of $\text{Ag}_{1-x/2}\text{Bi}_{1-x/2}\text{Sn}_x\text{Se}_2$ gradually increases with the increasing Sn ratio. It is clear that the carrier type change is related to the doping of Sn. The most likely reason for this phenomenon is that the participation of Sn modifies the intrinsic point defects of $\text{Ag}_{1-x/2}\text{Bi}_{1-x/2}\text{Sn}_x\text{Se}_2$. However, it is very difficult to confirm this conjecture from theoretical calculations or experiment measurements due to the disordered atomic distribution of these materials. The electrical conductivity of Sn-doped AgBiSe_2 falls in the range from 110 S/cm to 150 S/cm at 773 K, which is comparable with cubic $(\text{AgBiSe}_2)_{1-x}(\text{PbSe})_x$ [32]. Due to the change of carrier type, an extreme power factor (PF) value is observed at about 373 K. The maximum PF value of the $\text{Ag}_{1-x/2}\text{Bi}_{1-x/2}\text{Sn}_x\text{Se}_2$ materials with p -type transport properties is about $0.8 \mu\text{W}/\text{cm}\cdot\text{K}^2$, while $\text{Ag}_{0.875}\text{Bi}_{0.875}\text{Sn}_{0.25}\text{Se}_2$ exhibits the maximum n -type PF value of $\sim 1.2 \mu\text{W}/\text{cm}\cdot\text{K}^2$ at 773 K.

The measured total thermal conductivity of $\text{Ag}_{1-x/2}\text{Bi}_{1-x/2}\text{Sn}_x\text{Se}_2$ samples is shown in Figure 6a. The room temperature thermal conductivity of $\text{Ag}_{1-x/2}\text{Bi}_{1-x/2}\text{Sn}_x\text{Se}_2$ ranges from 0.5–0.6 W/m·K, lower than the measured thermal conductivity of pristine AgBiSe_2 due to the enhanced point defect scattering. It should be noticed that the thermal conductivity of Sn-doped samples is inclined to contain less bipolar contribution due to the coexistence of holes and electrons. The thermal conductivity contributed from lattice vibration (κ_{latt}) and bipolar effect (κ_{bip}) is calculated by subtracting the electronic thermal conductivity from total thermal conductivity. The electronic thermal conductivity (κ_{ele}) is estimated by using the formula $\kappa_{\text{ele}} = L\sigma T$, where L , σ , and T are the Lorenz factor, electrical conductivity, and absolute temperature, respectively. The Lorenz factors are calculated using a single parabolic band (SPB) model [41]. Considering that $\text{Ag}_{1-x/2}\text{Bi}_{1-x/2}\text{Sn}_x\text{Se}_2$ materials may exhibit multiple band behaviour, so the SPB model can only provide approximate estimates in this work. Figure 6b shows the calculated $\kappa_{\text{latt}} + \kappa_{\text{bip}}$ results in the range of 300 K to 773 K. Due to the enhanced point defects scattering, the lattice thermal conductivity of Sn-doped AgBiSe_2 is lower than that of pristine AgBiSe_2 in the range from 300 K to 523 K. The $\kappa_{\text{latt}} + \kappa_{\text{bip}}$ values of $\text{Ag}_{0.9}\text{Bi}_{0.9}\text{Sn}_{0.2}\text{Se}_2$, $\text{Ag}_{0.875}\text{Bi}_{0.875}\text{Sn}_{0.25}\text{Se}_2$, and $\text{Ag}_{0.825}\text{Bi}_{0.825}\text{Sn}_{0.35}\text{Se}_2$ are in the range of 0.45–0.6 W/m·K, while that of $\text{Ag}_{0.85}\text{Bi}_{0.85}\text{Sn}_{0.3}\text{Se}_2$ is much lower (only 0.37 W/m·K at 773 K). Such a low thermal conductivity is comparable with previous studies of cubic AgBiSe_2 materials [32–34]. This ultra-low $\kappa_{\text{latt}} + \kappa_{\text{bip}}$ value can be explained by two reasons, namely the increased point defect scattering caused by doping Sn and the increased phonon–phonon scattering with increasing temperature. Figure 7 presents the calculated ZT values of the $\text{Ag}_{1-x/2}\text{Bi}_{1-x/2}\text{Sn}_x\text{Se}_2$ samples. The final ZT values are very low compared with state-of-the-art thermoelectric materials, ranging from 0.06 to 0.14 at 773 K. However, due to the high structural symmetry and low thermal conductivity of these materials, $\text{Ag}_{1-x/2}\text{Bi}_{1-x/2}\text{Sn}_x\text{Se}_2$ can still be viewed as a potential thermoelectric material candidate.

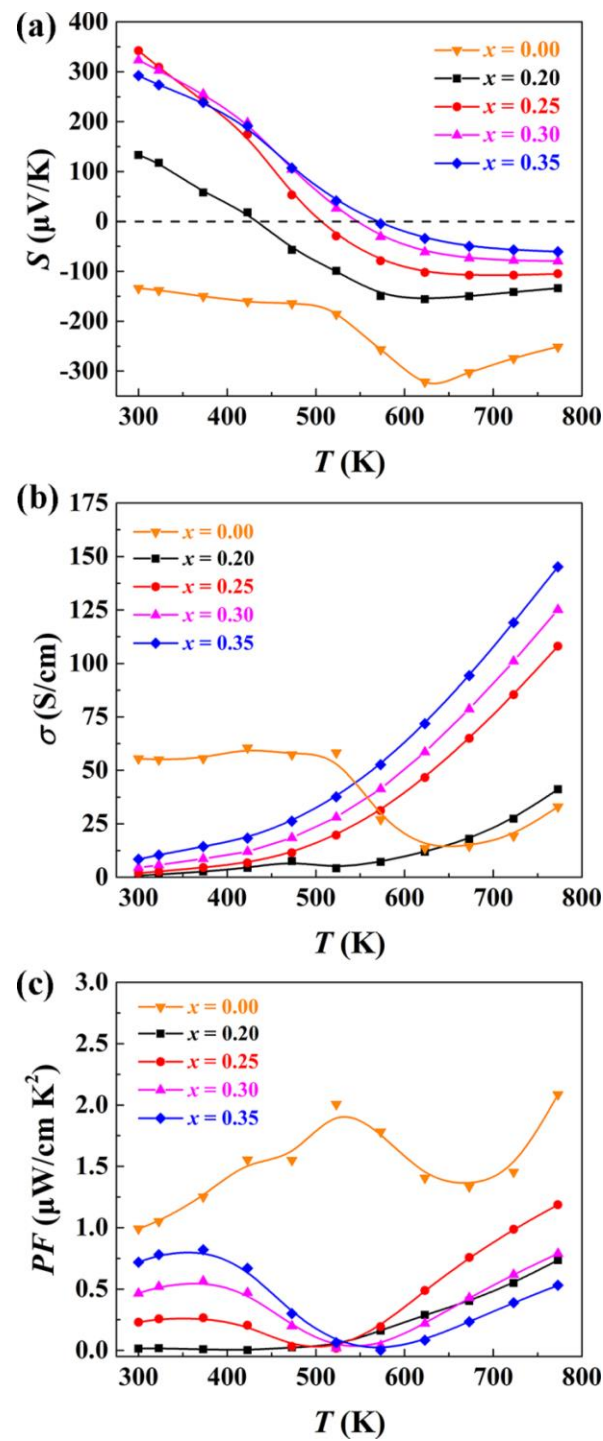


Figure 5. (a) Seebeck coefficient, (b) electrical conductivity, and (c) power factor of $\text{Ag}_{1-x/2}\text{Bi}_{1-x/2}\text{Sn}_x\text{Se}_2$ samples measured from room temperature to 773 K.

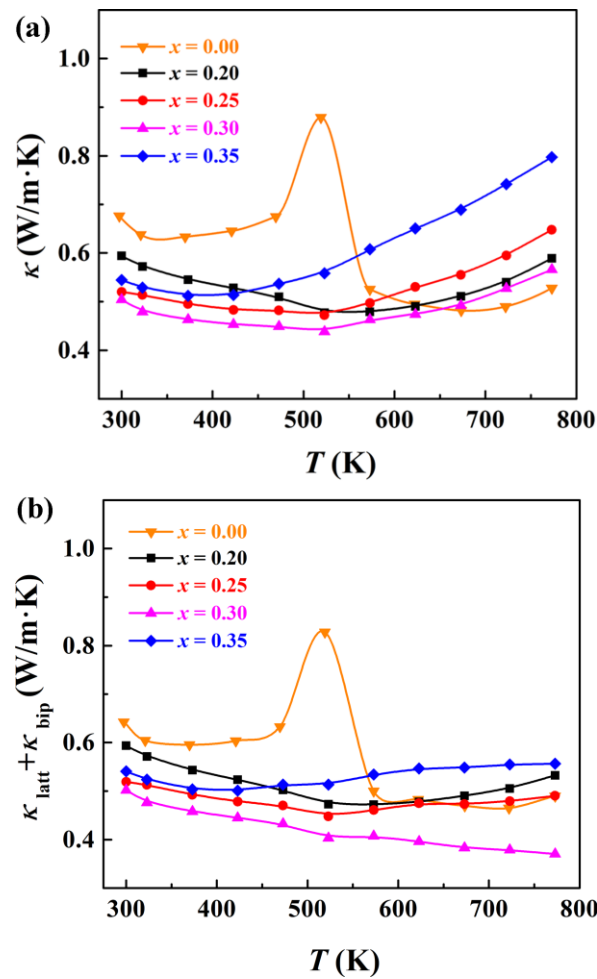


Figure 6. (a) Thermal conductivity of $\text{Ag}_{1-x/2}\text{Bi}_{1-x/2}\text{Sn}_x\text{Se}_2$ samples measured from room temperature to 773 K, and (b) sum of lattice thermal conductivity and bipolar thermal conductivity.

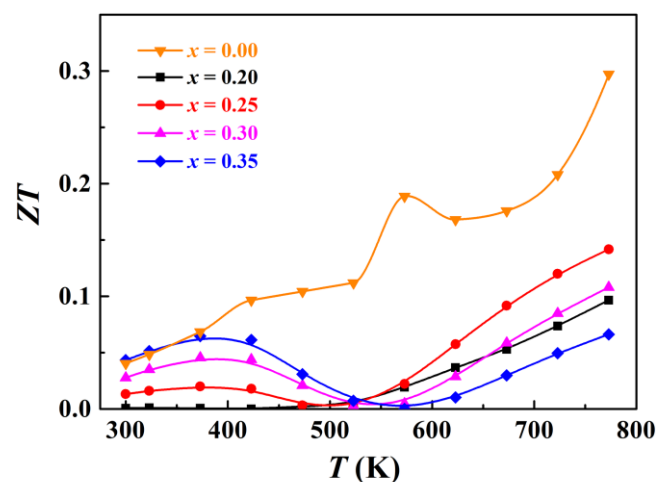


Figure 7. Temperature dependent ZT values for $\text{Ag}_{1-x/2}\text{Bi}_{1-x/2}\text{Sn}_x\text{Se}_2$.

4. Conclusions

In summary, the polymorph changes and thermoelectric properties of Sn-doped AgBiSe_2 were investigated. The room-temperature crystal structure of $\text{Ag}_{1-x/2}\text{Bi}_{1-x/2}\text{Sn}_x\text{Se}_2$ was transformed from a hexagonal structure to a disordered cubic structure when the value of x was larger than 0.20. In addition, the carrier type of $\text{Ag}_{1-x/2}\text{Bi}_{1-x/2}\text{Sn}_x\text{Se}_2$ at room

temperature was *p*-type, in contrast to the the *n*-type conductivity of pristine AgBiSe₂. The electrical conductivity exponentially increased with increasing temperature. The thermal conductivity of Ag_{1-x/2}Bi_{1-x/2}Sn_xSe₂ was ultra-low (in the range of 0.4 to 0.8 W/m·K) over the entire measured temperature range. Due to its high structural symmetry and low thermal conductivity, Ag_{1-x/2}Bi_{1-x/2}Sn_xSe₂ is a potentially lead-free thermoelectric material candidate. However, further in-depth investigation into enhancing the power factor of this material will be necessary.

Supplementary Materials: The following are available online at <https://www.mdpi.com/article/10.3390/cryst11091016/s1>. Figure S1: SEM image and related EDS mapping; Figure S2: rietveld analysis; Figure S3: $\ln \rho$ versus $1/T$.

Author Contributions: Conceptualization, X.-C.L.; formal analysis, X.-C.L.; writing—original draft preparation, X.-C.L.; writing—review and editing, X.-C.L. and M.-Y.P. All authors have read and agreed to the published version of the manuscript.

Funding: This research was funded by National Natural Science Foundation of China (grant no. 21601021) and Start-Up Foundation of Shandong Jiaotong University (grant no. BS2018027).

Conflicts of Interest: The authors declare no conflict of interest.

References

- Shi, X.; Chen, L. Thermoelectric materials step up. *Nat. Mater.* **2016**, *15*, 691–692. [CrossRef]
- Sootsman, J.R.; Chung, D.Y.; Kanatzidis, M.G. New and old concepts in thermoelectric materials. *Angew. Chem. Int. Ed.* **2009**, *48*, 8616–8639. [CrossRef]
- Zhao, X.; Zhao, L.D. Thermoelectric materials: Energy conversion between heat and electricity. *J. Mater.* **2015**, *1*, 92–105.
- Liu, K.-F.; Xia, S.-Q. Recent progresses on thermoelectric Zintl phases: Structures, materials and optimization. *J. Solid State Chem.* **2019**, *270*, 252–264. [CrossRef]
- Brown, S.R.; Kauzlarich, S.M.; Gascoin, F.; Snyder, G.J. Yb₁₄MnSb₁₁: New High Efficiency Thermoelectric Material for Power Generation. *Chem. Mater.* **2006**, *18*, 1873–1877. [CrossRef]
- Liu, H.; Shi, X.; Xu, F.; Zhang, L.; Zhang, W.; Chen, L.; Li, Q.; Uher, C.; Day, T.; Snyder, G.J. Copper ion liquid-like thermoelectrics. *Nat. Mater.* **2012**, *11*, 422–425. [CrossRef]
- Bai, H.; Su, X.; Yang, D.; Zhang, Q.; Tan, G.; Uher, C.; Tang, X.; Wu, J. An instant change of elastic lattice strain during Cu₂Se phase transition: Origin of abnormal thermoelectric properties. *Adv. Funct. Mater.* **2021**, *31*, 2100431. [CrossRef]
- Prado-Gonjal, J.; López, C.A.; Pinacca, R.M.; Serrano-Sánchez, F.; Nemes, N.M.; Dura, O.J.; Martínez, J.L.; Fernández-Díaz, M.T.; Alonso, J.A. Correlation between Crystal Structure and Thermoelectric Properties of Sr_{1-x}Ti_{0.9}Nb_{0.1}O_{3-δ} Ceramics. *Crystals* **2020**, *10*, 100. [CrossRef]
- Chen, Y.-X.; Shi, K.-D.; Li, F.; Xu, X.; Ge, Z.-H.; He, J. Highly enhanced thermoelectric performance in BiCuSeO ceramics realized by Pb doping and introducing Cu deficiencies. *J. Am. Ceram. Soc.* **2019**, *102*, 5989–5996. [CrossRef]
- Valencia-Gálvez, P.; Delgado, D.; López, M.L.; Álvarez-Serrano, I.; Moris, S.; Galdámez, A. AgSn[Bi_{1-x}Sb_x]Se₃: Synthesis, Structural Characterization, and Electrical Behavior. *Crystals* **2021**, *11*, 864. [CrossRef]
- Hoang, K.; Mahanti, S.D. Atomic and electronic structures of I-V-VI₂ ternary chalcogenides. *J. Sci. Adv. Mater. Dev.* **2016**, *1*, 51–56. [CrossRef]
- Morelli, D.T.; Jovic, V.; Heremans, J.P. Intrinsically Minimal Thermal Conductivity in Cubic I–V–VI₂ Semiconductors. *Phys. Rev. Lett.* **2008**, *101*, 035901. [CrossRef]
- Skoug, E.J.; Morelli, D.T. Role of Lone-Pair Electrons in Producing Minimum Thermal Conductivity in Nitrogen-Group Chalcogenide Compounds. *Phys. Rev. Lett.* **2011**, *107*, 235901. [CrossRef]
- Du, B.; Zhang, R.; Chen, K.; Mahajan, A.; Reece, M.J. The impact of lone-pair electrons on the lattice thermal conductivity of the thermoelectric compound CuSbS₂. *J. Mater. Chem. A* **2017**, *5*, 3249–3259. [CrossRef]
- Wang, H.; Li, J.-F.; Zou, M.; Sui, T. Synthesis and transport property of AgSbTe₂ as a promising thermoelectric compound. *Appl. Phys. Lett.* **2008**, *93*, 202106. [CrossRef]
- Liu, X.-C.; Wang, Y.-M.; Qi, M.-L.; Pan, M.-Y. Enhanced thermoelectric properties in Ag-rich AgSbSe₂. *J. Solid State Chem.* **2020**, *288*, 121454. [CrossRef]
- Hong, M.; Chen, Z.-G.; Yang, L.; Liao, Z.-M.; Zou, Y.-C.; Chen, Y.-H.; Matsumura, S.; Zou, J. Achieving $zT > 2$ in *p*-Type AgSbTe_{2-x}Se_x Alloys via Exploring the Extra Light Valence Band and Introducing Dense Stacking Faults. *Adv. Energy Mater.* **2018**, *8*, 1702333. [CrossRef]
- Guin, S.N.; Chatterjee, A.; Negi, D.S.; Datta, R.; Biswas, K. High thermoelectric performance in tellurium free *p*-type AgSbSe₂. *Energy Environ. Sci.* **2013**, *6*, 2603–2608. [CrossRef]
- Zhou, J.; Bian, G.; Zhu, Q.; Zhang, Y.; Li, C.; Dai, J. Solvothermal crystal growth of CuSbQ₂ (Q = S, Se) and the correlation between macroscopic morphology and microscopic structure. *J. Solid State Chem.* **2009**, *182*, 259–264. [CrossRef]

20. Kyono, A.; Kimata, M. Crystal structures of chalcostibite (CuSbS_2) and emplectite (CuBiS_2): Structural relationship of stereochemical activity between chalcostibite and emplectite. *Am. Mineral.* **2005**, *90*, 162–165. [[CrossRef](#)]
21. Geller, S.; Wernick, J.H. Ternary semiconducting compounds with sodium chloride-like structure: AgSbSe_2 , AgSbTe_2 , AgBiS_2 , AgBiSe_2 . *Acta Crystallogr.* **1959**, *12*, 46–54. [[CrossRef](#)]
22. Pinsker, Z.G.; Imamov, R.M. Electron diffraction study of the compound AgBiTe_2 . *Sov. Phys. Crystallogr.* **1964**, *9*, 277–280.
23. Glatz, A.C.; Pinella, A. X-ray and neutron diffraction studies of the high-temperature beta-phase of the $\text{AgBiSe}_2/\text{AgBiS}_2$ system. *J. Mater. Sci.* **1968**, *3*, 498–501. [[CrossRef](#)]
24. Pringle, G.J.; Thorpe, R.I. Bohdanowiczite, juninite and laitakarite from the Kidd Creek mine, Timmins, Ontario. *Can. Mineral.* **1980**, *18*, 353–360.
25. Bayliss, P. Crystal chemistry and crystallography of some minerals in the tetradymite group. *Am. Mineral.* **1991**, *76*, 257–265.
26. Liu, X.; Jin, D.; Liang, X. Enhanced thermoelectric performance of n-type transformable AgBiSe_2 polymorphs by indium doping. *Appl. Phys. Lett.* **2016**, *109*, 133901. [[CrossRef](#)]
27. Pan, L.; Bérardan, D.; Dragoe, N. High Thermoelectric Properties of n-Type AgBiSe_2 . *J. Am. Chem. Soc.* **2013**, *135*, 4914–4917. [[CrossRef](#)]
28. Wu, H.-J.; Wei, P.-C.; Cheng, H.-Y.; Deng, J.-R.; Chen, Y.-Y. Ultralow thermal conductivity in n-type Ge-doped AgBiSe_2 thermoelectric materials. *Acta Mater.* **2017**, *141*, 217–229. [[CrossRef](#)]
29. Guin, S.N.; Srihari, V.; Biswas, K. Promising thermoelectric performance in n-type AgBiSe_2 : Effect of aliovalent anion doping. *J. Mater. Chem. A* **2015**, *3*, 648–655. [[CrossRef](#)]
30. Parker, D.S.; May, A.F.; Singh, D.J. Benefits of Carrier-Pocket Anisotropy to Thermoelectric Performance: The Case of p-Type AgBiSe_2 . *Phys. Rev. Appl.* **2015**, *3*, 064003. [[CrossRef](#)]
31. Li, S.; Feng, Z.; Tang, Z.; Zhang, F.; Cao, F.; Liu, X.; Singh, D.J.; Mao, J.; Ren, Z.; Zhang, Q. Defect Engineering for Realizing p-Type AgBiSe_2 with a Promising Thermoelectric Performance. *Chem. Mater.* **2020**, *32*, 3528–3536. [[CrossRef](#)]
32. Zhu, H.; Zhao, T.; Zhang, B.; An, Z.; Mao, S.; Wang, G.; Han, X.; Lu, X.; Zhang, J.; Zhou, X. Entropy Engineered Cubic n-Type AgBiSe_2 Alloy with High Thermoelectric Performance in Fully Extended Operating Temperature Range. *Adv. Energy Mater.* **2021**, *11*, 2003304. [[CrossRef](#)]
33. Sudo, K.; Goto, Y.; Sogabe, R.; Hoshi, K.; Miura, A.; Moriyoshi, C.; Kuroiwa, Y.; Mizuguchi, Y. Doping-Induced Polymorph and Carrier Polarity Changes in Thermoelectric $\text{Ag}(\text{Bi,Sb})\text{Se}_2$ Solid Solution. *Inorg. Chem.* **2019**, *58*, 7628–7633. [[CrossRef](#)]
34. Bernges, T.; Peilstöcker, J.; Dutta, M.; Ohno, S.; Culver, S.P.; Biswas, K.; Zeier, W.G. Local Structure and Influence of Sb Substitution on the Structure–Transport Properties in AgBiSe_2 . *Inorg. Chem.* **2019**, *58*, 9236–9245. [[CrossRef](#)] [[PubMed](#)]
35. Li, J.; Pan, Y.; Wu, C.; Sun, F.; Wei, T. Processing of advanced thermoelectric materials. *Sci. China Technol. Sci.* **2017**, *60*, 1347–1364. [[CrossRef](#)]
36. Atsushi, O.; Ikuhiko, U. The Crystal Structure of Stannous Selenide SnSe . *J. Phys. Soc. Jpn.* **1956**, *11*, 470.
37. Rodríguez-Carvajal, J. Recent Advances in Magnetic Structure Determination by Neutron Powder Diffraction. *Phys. B* **1993**, *192*, 55–69. [[CrossRef](#)]
38. Shannon, R.D. Revised Effective Ionic Radii and Systematic Studies of Interatomic Distances in Halides and Chalcogenides. *Acta Cryst.* **1976**, *A32*, 751. [[CrossRef](#)]
39. Mariano, A.N.; Chopra, K.L. Polymorphism in some IV-VI compounds induced by high pressure and thin epitaxial growth. *Appl. Phys. Lett.* **1967**, *10*, 282–284. [[CrossRef](#)]
40. Voroshilov, Y.V.; Cholovej, M.I.; Potorii, M.V. The X-ray analysis of the combinations AgAsSe_2 and Ag_3AsSe_3 . *Kristallografiya* **1976**, *21*, 585–586.
41. May, A.F.; Singh, D.J.; Snyder, G.J. Influence of band structure on the large thermoelectric performance of lanthanum telluride. *Phys. Rev. B* **2009**, *79*, 153101. [[CrossRef](#)]